Journal of Manufacturing Processes 113 (2024) 47–60

Contents lists available at ScienceDirect

Journal of Manufacturing Processes

journal homepage: www.elsevier.com/locate/manpro

3D numerical modelling of residual stresses induced by reaming

Timothé Leveille [a], Frédéric Valiorgue [a], Maxime Dumas [b], Ugo Masciantonio [c], Alexandre Brosse [d], Habib Karaouni [e], Joel Rech [a,*]

[a] Université de Lyon, Ecole Centrale de Lyon – ENISE, LTDS, UMR CNRS 5513, 58 rue Jean Parot, 42100 Saint-Etienne, France
[b] Airbus Helicopters, Laboratoire Materiaux Procédés, Aeroport Marseille Provence, 13725 Marignane, France
[c] Cetim, 7 rue de la presse, 42952 Saint-Etienne, France
[d] Framatome, 10 Rue Juliette Recamier, 69456 Lyon, France
[e] SAFRAN Tech, Rue des Jeunes-Bois, 78772 Magny-les-Hameaux, France

ARTICLE INFO

Keywords:
Reaming
Residual stress
Numerical modelling

ABSTRACT

The fatigue life of safety components is a major issue for many economic sectors, including aeronautics and energy. In the scientific literature, the link between surface integrity, particularly residual stresses, and fatigue life has long been established. The objective of this paper is to predict the residual stresses induced by a reaming operation using a solid reamer. Previous works proposed a method to predict the residual stresses induced by a turning operation. This method, implemented in a finite element code, is based on the application of equivalent 3D thermomechanical loadings onto the final surface of a part. The method is called 'hybrid' because it uses experimental measurements of the cutting forces to calibrate the intensity of the thermomechanical loadings. This paper aims at adapting this 3D hybrid modelling method to the case of a reaming operation in a martensitic stainless steel. The model only considers the effects of major cutting edges and not the effects of the margins. A comparison between the numerical results and the experimental residual stresses measured from X-ray diffraction shows good accuracy of the model. It is revealed that the reaming operation has a significant effect on the residual stress state on the surface and that its action is dominated by plastic deformation, leading to compressive stresses.

1. Introduction

The fatigue life of safety components is a major issue for many economic sectors, including aeronautics and energy. The manufacturing processes, and especially the machining processes, involved in the production of these components are key elements responsible for the fatigue resistance [1]. Machining processes affects the 'surface integrity' [2] that includes microstructure, roughness and residual stresses at the surface. [3] summarised several works which showed that cutting processes are responsible for severe changes in surface integrity. This paper only focuses on the generation of residual stresses. During a machining operation, residual stresses are generated by the plastic deformation and high temperatures that occur simultaneously on the machined surface, while the rest of the part remains at room temperature [3].

This paper focuses on reaming operations with solid carbide tools (Fig. 1). Reaming is a finishing operation, commonly used for many critical components, especially in the aerospace industry. A reamer removes a few microns from the part by using several cutting edges. It is often performed after a drilling operation and, sometimes, after a boring operation. Reaming with a solid carbide reamer is an operation that has received little interest from the scientific community. Regarding the analysis of the residual stress state after reaming, some authors assume, without proof, that reaming does not modify the surface residual stress state. According to these authors, it only modifies the redistribution of residual stresses which were previously present in the bulk of the material or that were generated by the previous drilling operation [5] or cold expansion operation [4]. On the contrary, the work of [6] showed that reaming induces compressive residual stresses in both directions (circumferential and axial directions), over a depth of 50 to 100 μm (Fig. 1). Furthermore, [6] showed that reaming induces its own residual stress signature on the final surface and that previous operations (drilling, boring) do not influence the final state in this outer layer.

During a reaming operation, residual stresses are first generated by the major cutting edges (6 teeth in the case of the reamer in Fig. 2), and then by the 6 margins rubbing on the surface previously generated by the cutting edges. This constitutes 12 (6 + 6) zones in which the

* Corresponding author.
E-mail address: joel.rech@enise.fr (J. Rech).

https://doi.org/10.1016/j.jmapro.2024.01.050
Received 16 July 2023; Received in revised form 4 January 2024; Accepted 18 January 2024

machined surface is plastically deformed and heated during each revolution. In Fig. 2, the reamer machines from top to bottom and then exits from the hole; the reamer then has to return to its original position over the part. This causes a third contact [6], which may change the final residual stress state. So, the final residual stress state is induced by the sequential effects of 3 contacts. The configuration is very different from a turning operation (the most investigated case study in the scientific literature) in which the cutting tool has only a single contact zone and does not return over the previously machined surface.

The objective of this paper is to propose a method to model the residual stress state induced by a reaming operation with a solid carbide reamer. In particular, this paper only models the effects of major cutting edges. The effects of the margins are not considered. The effect of the reamer's ascent is not considered. The purpose of the proposed model, therefore, is to predict the influence of a multi-teeth rotating axial tool that removes a thin layer.

As far as residual stress modelling is concerned, no scientific paper has addressed the reaming application. On the contrary, a huge number of models have been developed for turning applications. Historically, 2D analytical models such as those developed by [7] were the most popular as they provide rapidly qualitative results with a short time. However, these analytical models have strong assumptions that limits their ability to provide quantitative results. So, several researchers proposed numerical models thanks to the development of computational capabilities. For instance, [8] have used a numerical Lagrangian formulation in orthogonal cutting. Such models assume that the cutting operation can be considered as a 2D plain strain configuration, which is far from a 3D industrial longitudinal cutting operation. The second issue comes from the high strain around the cutting edge radius (separation) that leads to mesh distortions as highlighted by [9]. The third issue comes from the weak modelling of friction at the boundaries of two Lagrangian meshed solids in movement as explained in [10]. As a consequence, [11] have also used 2D Arbitrary Lagrangian Eulerian (A.L.E) formulation to improve mesh distortion and contact modelling issues. Unfortunately, as these works use an explicit time integration algorithm, they lead to difficulties in modelling the relaxation time (crucial for residual stress prediction). Finally, even these 2D models are of scientific interest to understand the mechanisms leading to residual stresses in an orthogonal cutting configuration, the industrial interest is related to 3D surfaces generated by a large number of revolutions (longitudinal turning). Indeed, the cutting tool modifies the residual stress state obtained during the previous revolutions. As shown by [12], several cutting revolutions are necessary to reach a steady state in turning. So, some researchers, such as [13], proposed a 3D Lagrangian formulation to predict residual stresses in cutting. This paper brings a better understanding of the physical phenomena leading to residual stress generation. More recently, [14] introduce a Coupled Eulerian Lagrangian

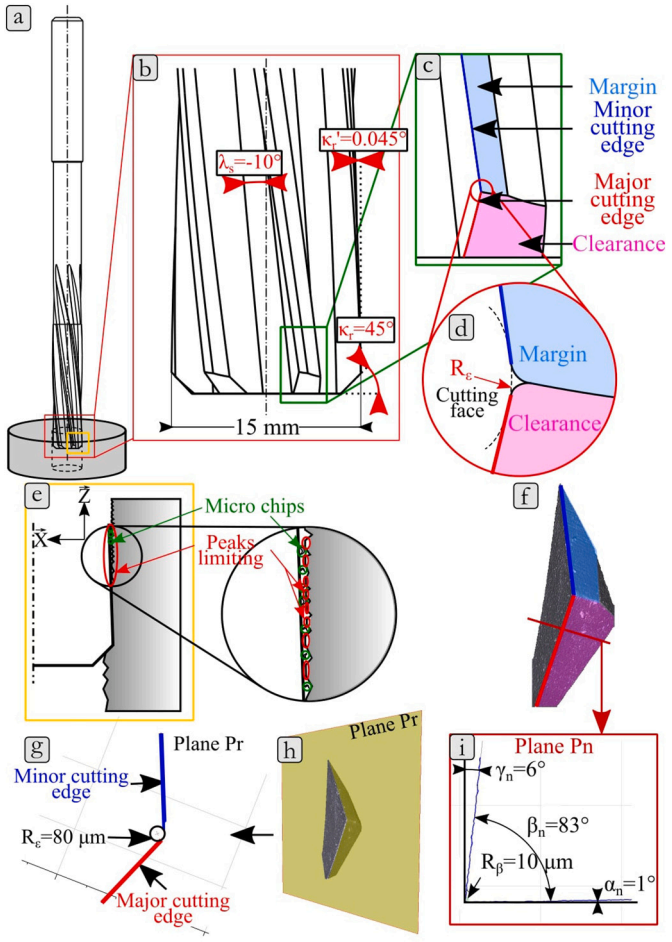

Fig. 2. Presentation of a reaming operation (a) with the various active parts of the cutting edges (b, c and d), the action of the margins (e), and the various angles in the planes Pn (f and i) and Pr (h).

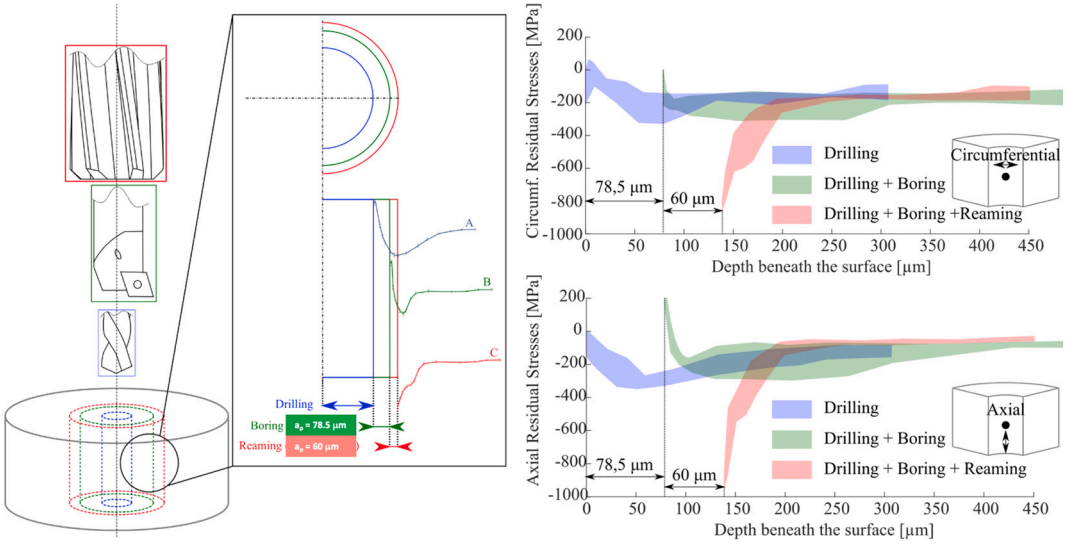

Fig. 1. Comparison of various machining sequence (drilling ≥ Boring ≥ Reaming) on the residual stress state of a 15-5PH martensitic stainless steel (since [6]).

approach. However, the previous weaknesses of the Lagrangian formulation remain, and the computational time is not realistic for industry. An alternative approach proposed by [15], and improved by [16], consists in modelling the residual stress generation by removing the chip formation and cutting tool modelling and replacing it with equivalent thermo-mechanical loadings (Fig. 3). These equivalent loadings are moved onto the machined surface with a velocity equal to the cutting speed during several revolutions on the machined surface. The loadings induce high local temperatures and severe local plastic deformation in the near surface, whereas the bulk of the part remains unaffected. These temperature and plastic deformation gradients are responsible for residual stress generation in the near surface. The shapes of the thermo-mechanical loadings are determined by several 2D orthogonal cutting simulations along the cutting edge. The loading intensity is calibrated using force measurements during the machining operation. This combination of an experimental and a numerical approach means that it is a 'hybrid method'. After the cooling phase, this model makes residual stress prediction possible. This hybrid model for residual stress prediction, based on an implicit formulation, presents advantages like the absence of highly distorted mesh, the possibility to obtain accurate mechanical equilibrium computation and the possibility of 3D multi-revolution simulations that is necessary to reach a steady state in residual stress generation.

The present work aims at proposing a numerical model of residual stress generation in solid reaming by adapting the method developed by [16] for the case of longitudinal finishing turning. The method will be applied on a reaming operation in a martensitic stainless steel 15-5PH with a solid carbide reamer.

2. Technical study of reaming

Reaming is a finishing operation for enlarging and calibrating the diameter of a cylindrical surface. It is performed with a solid carbide reamer (Fig. 2a) and aims to remove a few micrometers (a_p: 50–500 µm). The reamer is composed of several cutting edges (6 edges in the case of Fig. 2a), followed by 6 margins (Fig. 2a). The purpose of each cutting edges is to remove material. The material removal is influenced by the lead angle K_r (Fig. 2b), the tool inclination angle λ_s (Fig. 2b), the local rake angle γ_n (Fig. 2i), the corner radius R_ε (Fig. 2e) and the cutting edge radius R_β (Fig. 2i).

The margins are used to guide the tool (Fig. 2e). The action of the margins is influenced by their width and the back taper angle Kr' (Fig. 2b).

The cutting conditions of this process are very low compared to other cutting processes. Thus, the cutting speed V_c is a few m/min ($V_c = 5$–15 m/min) and the feed f ($f = 0.1$–0.5 mm/rev) is of the order of a few millimetres.

Regarding the generation of residual stresses, [17] showed that both parts, cutting edges and margins contribute to the generation of residual stresses. In the case of reaming 15-5PH martensitic stainless steel, the axial and circumferential stresses are in compression, with an affected depth of about 100 µm.

3. Residual stress modelling: a two-scale approach based on advanced equivalent thermomechanical loadings

We present a method for modelling the residual stress state induced by a reaming operation with a solid carbide tool. It is inspired by the method developed by [16], for the case of finishing by longitudinal turning, and is based on the identification of equivalent 3D thermo-mechanical loadings moving on the surface. The detailed description of the previous longitudinal turning model is available in [16]. It is recommended (but not mandatory) to read this paper to have a better understanding of the present paper.

Fig. 4 gives a rapid overview of the proposed reaming method. Then, in Section 3.1 to 3.6, each step is presented in detail.

First of all, the undeformed cut section (CS), generated by a single tooth out of 6 teeth, needs to be defined (Fig. 4b) by the geometry of the reamer (κ_r, R_ε) and the cutting conditions (f_z, a_p). Then, this section is divided into several elementary 2D orthogonal sections, named $S_{(i)}$. Each section $S_{(i)}$ has an uncut chip thickness $h_{(i)}$. In each elementary section $S_{(i)}$, the material removal can be simulated by a 2D finite element model in ABAQUS Explicit (Fig. 4c).

NB: It is assumed that each 2D section is independent from its neighbours. This strong assumption has been validated for turning by [16].

In each 2D simulation, thermomechanical loadings are applied on the machined surface (Fig. 4c) and extracted along the 'extraction path' for each section $S_{(i)}$. The linear heat flux density distribution $\varphi_{th\text{-}2D(i)}$, the linear normal stress distribution $\sigma_{n\text{-}2D(i)}$ and the linear tangential stress distribution $\sigma_{t\text{-}2D(i)}$ are obtained along the extraction path. From these 2D thermomechanical loadings for each section $S_{(i)}$, the 3D thermo-mechanical loadings can be estimated: the heat flux distribution $\varphi_{th\text{-}3D\text{-}appro}$, the normal stress distribution $\sigma_{n\text{-}3D\text{-}appro}$ and the tangential stress distribution $\sigma_{t\text{-}3D\text{-}appro}$ (Fig. 4e). This 3D thermomechanical loading distribution is the combination of Fig. 4b (position of each section in the plane X-Z) and of Fig. 4c (the 2D thermomechanical loadings in the plane $e_{X(i)} - Y$).

However, the elementary 2D orthogonal cut models in ABAQUS are not able to accurately simulate thermomechanical loadings, as shown by [16]. The shapes of these thermomechanical loadings are considered to be acceptable, but not their magnitudes. Therefore, the magnitudes need to be calibrated and a so-called 'hybrid' method is used. The experimental forces (in the cutting direction $F_{Y(EXP)}$ and in the penetration direction $F_{Y(EXP)}$) (Fig. 4a) are measured for each tooth during a real reaming operation and compared with the numerical forces ($F_{Y\text{-}TOT}$(-NUM) in the cutting direction and $F_{eXX\text{-}TOT}$(NUM) in the penetration direction) (Fig. 4d). The ratio between the measured forces and the numerical forces provides two calibration factors (G_{FY} and G_{FX}) that enable calibration of the magnitude of the thermomechanical loadings (Fig. 4f). At this stage, the equivalent 3D thermomechanical loadings are known for a single pass, induced by a single tooth of the solid reamer. The next step

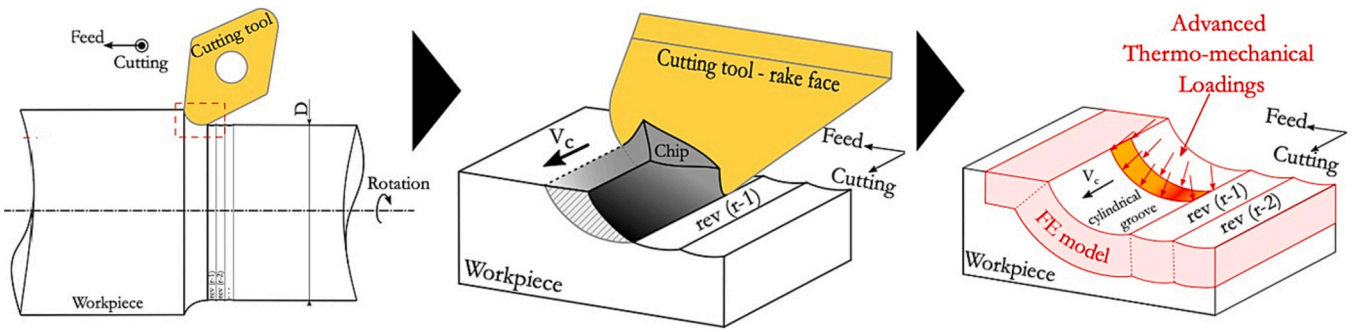

Fig. 3. Principle of the 3D hybrid model of residual stress generation in turning (since [16]).

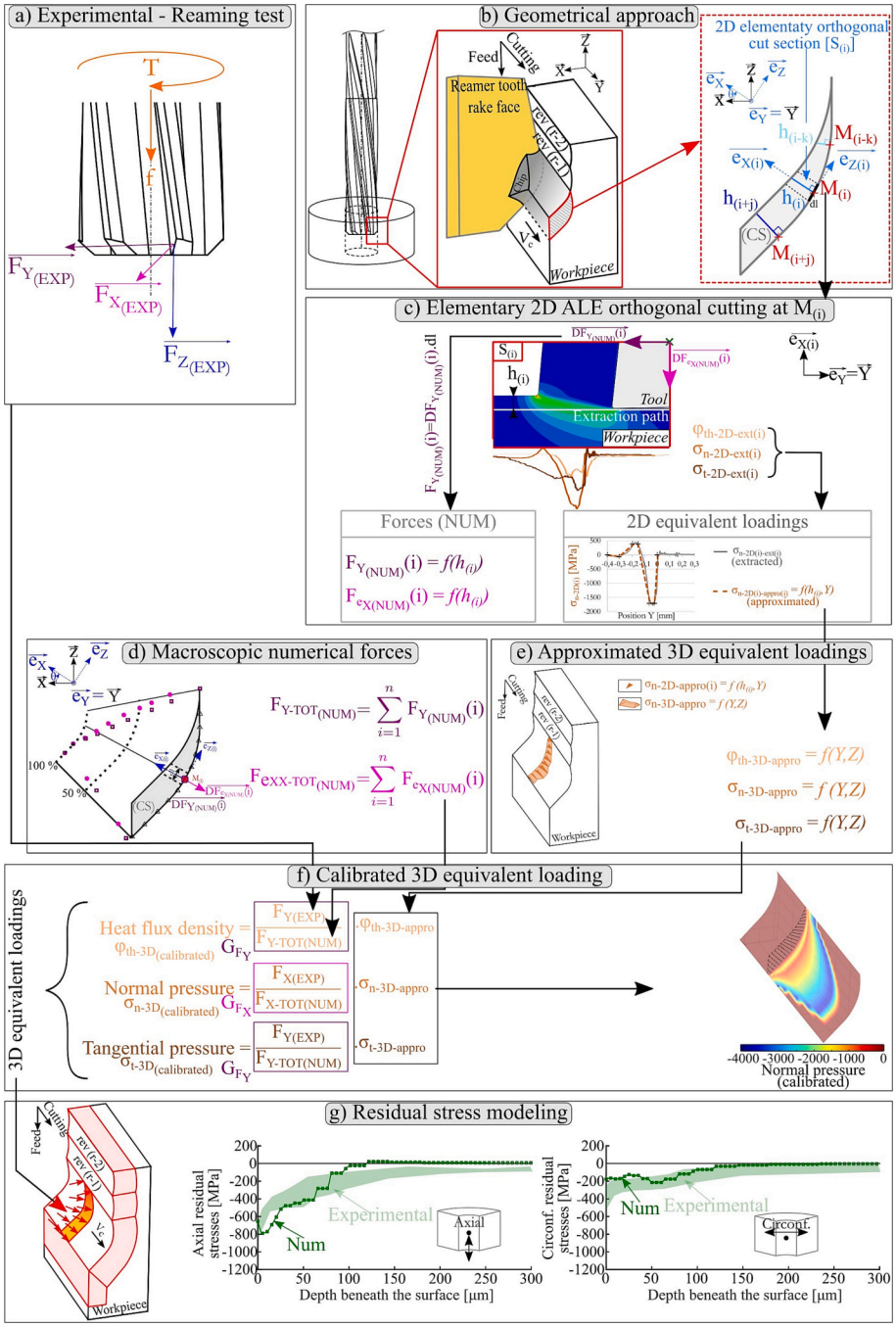

Fig. 4. Flowchart of the 3D hybrid method in solid reaming.

consists of moving the 3D calibrated thermomechanical loadings over the surface with a speed corresponding to the cutting speed V_c (Fig. 4f). As the solid reamer has 6 teeth, it is necessary to simulate several passes, in order to take into account the interactions between the passes, as shown by [16]. After the cooling step, the residual stresses can be quantified.

So a global overview of Fig. 4 shows that the model is based on 4 main steps:

- The undeformed cut section is divided in several 2D orthogonal cuts (assumed as independent from each other)
- The calculation of the 2D thermomechanical loadings of each 2D orthogonal cuts thanks to a well-known explicit 2D model in ABAQUS.
- The application of several 2D thermomechanical loadings on the curved machined surface, that creates the 3D thermomechanical loadings.
- The 3D loadings are then calibrated thanks to the experimental cutting force $F_{Y(EXP)}$ and penetration $F_{Y(EXP)}$)
- Finally residual stresses are computed in 3D thank to an implicit 3D model in SYSWELD. The 3D thermomechanical are moved other the machined surface during several revolutions until the model leads to a steady state in residual stress generation.

Each step is now described in detail.

3.1. Geometrical approach

Step 1 (Fig. 4b): the first step of the simulation method considers a single tooth (among 6) and a small volume of the real part. In Fig. 5, the strategy of the discretisation of the cutting edge is presented. First of all, a simplified machined part is defined (Fig. 5a). Then the undeformed cut section *CS* is obtained and can be discretised into several orthogonal sections (Fig. 5c).

The model of the machined part is defined in the reference system $S_R = (O, \vec{X}, \vec{Y}, \vec{Z})$ (Fig. 5). The volume and dimensions must be large enough to simulate residual stress generation at the centre without being disturbed by boundary effects. The base of the machined part is considered to be parallelepipedic. The curvature of the part is neglected, as the radius of the part is very large compared to the volume of the element being modelled. The initial surface is considered to be flat and the tool path is considered as linear. The tool generates a grooved surface with a radius equal to the corner radius R_ε of the tool (Fig. 5).

The undeformed cut section *CS* defined in the reference plane $(O, \vec{X}, \vec{Z})$ (Fig. 5) depends on:

- the cutting conditions (depth of cut a_p, feed per tooth f_z);
- the tool geometry (the corner radius R_ε, the lead angle κ_r).

The cutting edge is composed of a linear part and a curvilinear part. It is discretised with several points $M_{(i)}$, $i = 1$ to n, where n is the number of points. For each point $M_{(i)}$, a section $S_{(i)}$ is defined in a local reference $SL_{(i)} = \left(M_{(i)}, \vec{e}_{X(i)}, \vec{Y}, \vec{e}_{Z(i)}\right)$. Each section $S_{(i)}$ is defined by the locally undeformed chip thickness $h_{(i)}$, as well as the local rake angle $\gamma_{n(i)}$, the local clearance angle $\alpha_{n(i)}$, and the cutting-edge radius $R_{\beta(i)}$.

The two-coordinate systems S_R and $S_{L(i)}$ are related by the angle $\theta_{(i)} = \left(\vec{e}_{X(i)}, \vec{X}\right)$ (Fig. 5b).

Examples of the sections $S_{(i)}$ are shown in Fig. 5. In each section $S_{(i)}$, it is assumed that the tool performs an orthogonal cutting operation and that the sections are independent of each other.

In our case study, the local tool geometry is considered constant along the cutting edge: the clearance angle $\alpha_{(i)} = \alpha = 1°$, the rake angle $\gamma_{n(i)} = \gamma = 6°$ and the cutting-edge radius $R_{\beta(i)} = R_\beta = 10$ µm (Fig. 5). The tool inclination angle λ_s (helix angle) is considered to be negligible ($\lambda_s = 0$). These assumptions should be investigated in detail in a future paper.

3.2. Elementary 2D orthogonal cutting – ALE modelling

Step 2 (Fig. 4c): the material removal mechanisms are modelled for each section $S_{(i)}$ with a 2D orthogonal numerical cutting model. The 2D orthogonal model is based on the model developed by [18] in Abaqus ® Explicit. An Arbitrary Eulerian Lagrangian (ALE) formulation is used with an adaptive Lagrangian mesh. The elements used are CPE4RT for the tool and the material. The tool is modelled with only the properties of the carbide substrate, without considering the properties of the coating. Indeed, the few micrometre-thick coating is thermally transparent during a continuous cutting operation [19]. However, the influence of coating on friction and heat partition at the interface between the tool and the material is considered, in accordance with the equations proposed by [12].

The tool is considered to be rigid while the material part is deformable. The mesh is refined around the tool edge radius (Fig. 6) with a mesh size of 1 µm and the boundary conditions are shown in Fig. 6. More details on this 2D model can be found in [18]. The simulations in each section take 30 ms, until the steady state of the mechanical and geometrical parameters and heat flows are reached. This requires 120 h of computation, on a computer with a 3.2 GHz processor.

At the end of the simulation in section $S_{(i)}$, it is possible to obtain the 2D thermomechanical loadings that the tool applies on the machined surface (Fig. 7). These loadings can be extracted along the extraction path (Fig. 7a):

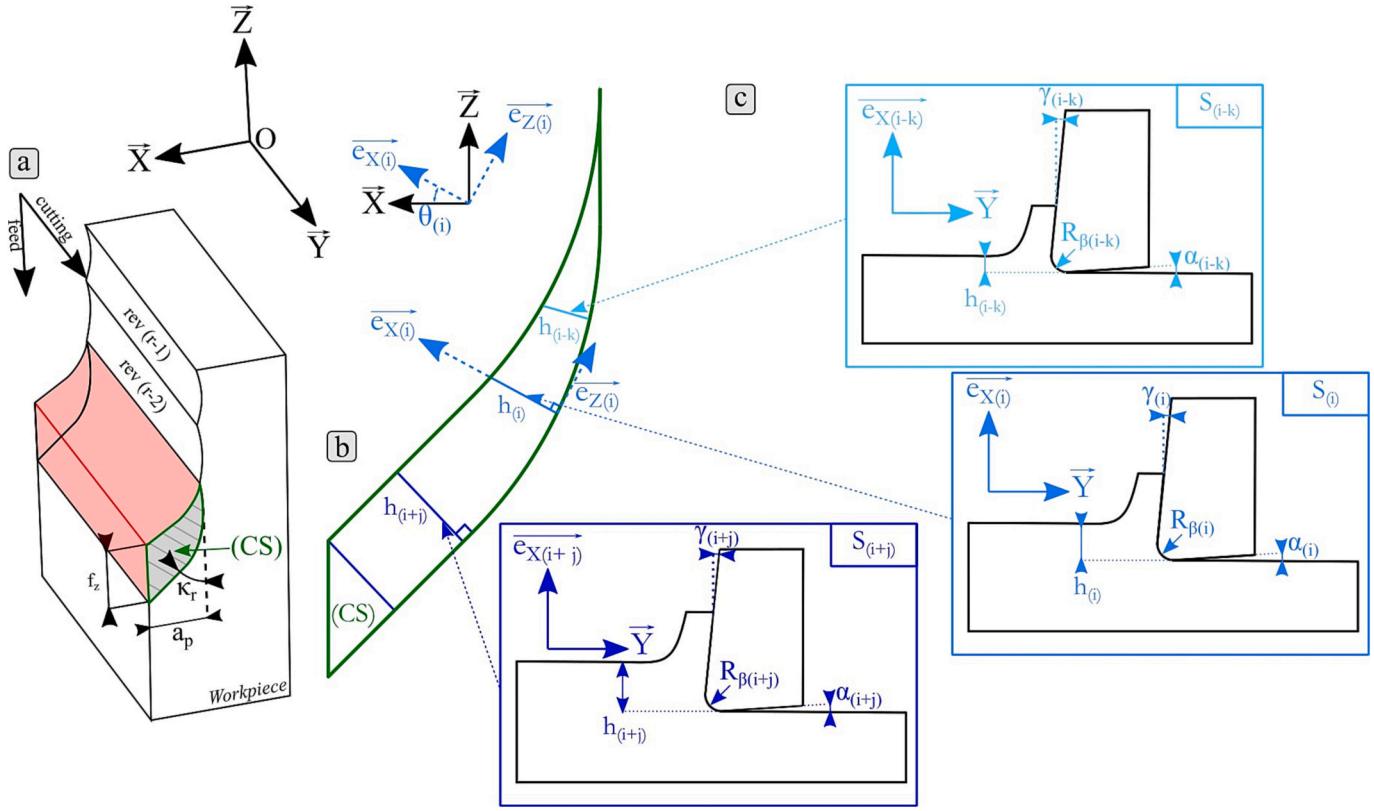

Fig. 5. The simplified machined part (a) with the theoretical undeformed cut section CS (b) discretised in various orthogonal cutting sections $S_{(i)}$ (c).

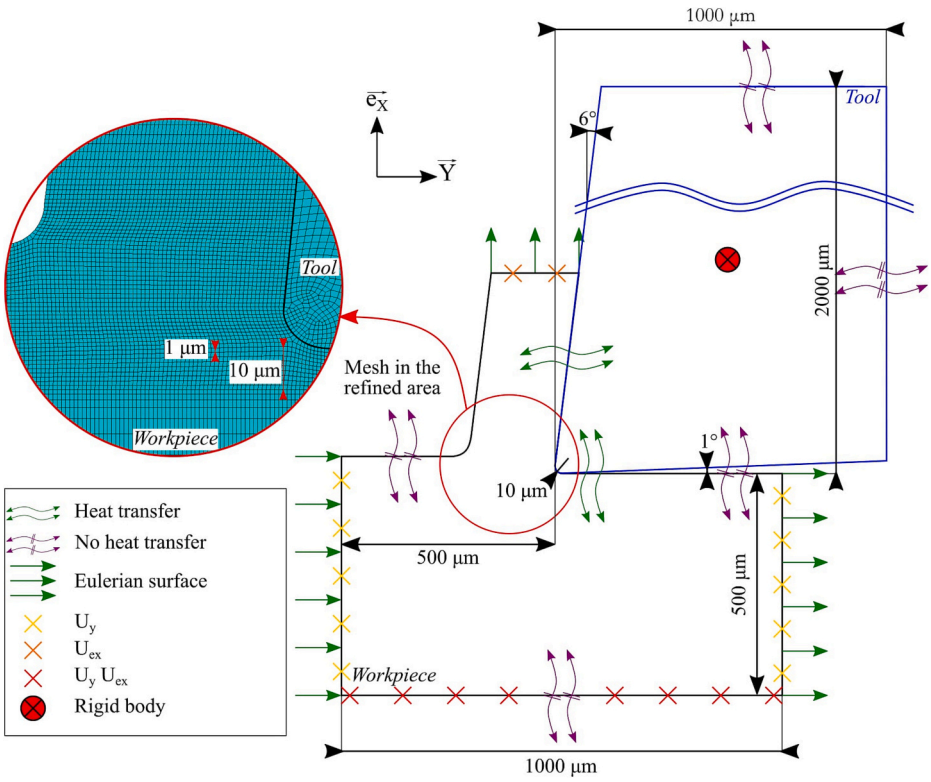

Fig. 6. 2D Elementary ALE cutting model.

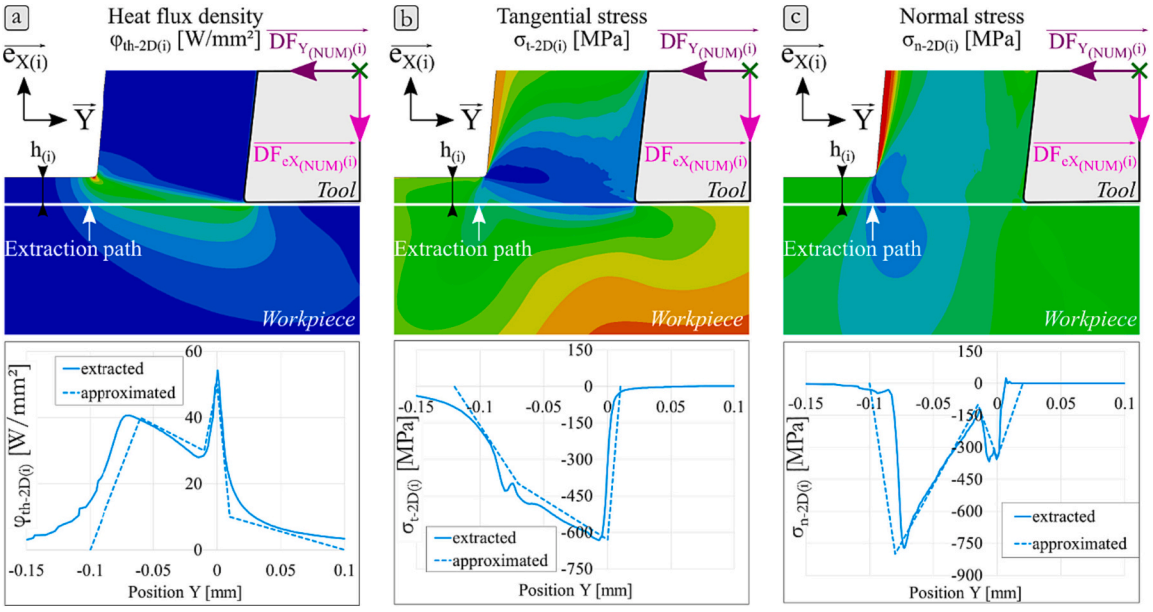

Fig. 7. 2D equivalent loadings extracted from the 2D ALE cutting model: a) the heat flux density, b) the tangential stress, and c) the normal stress distributions along the extraction path.

- The heat flux density $\varphi_{th-2D-ext(i)}$;
- The tangential stress $\sigma_{t-2D-ext(i)}$ parallel to $\overrightarrow{Y}$;
- The normal stress $\sigma_{n-2D-ext(i)}$ parallel to $\overrightarrow{e_{X(i)}}$.

The loading shapes are complex and must be simplified by straight lines, shown as dashed lines in Fig. 7.

Using all the loading shapes for each section $S_{(i)}$, it is possible to propose an equation between the loading shapes and the undeformed chip thickness $h_{(i)}$ (Eqs. (1)–(3)).

$$\varphi_{th-2D-appro(i)} = f(h(i), Y) \tag{1}$$

$$\sigma_{n-2D-appro(i)} = f(h(i), Y) \tag{2}$$

$$\sigma_{t-2D-appro(i)} = f(h(i), Y) \tag{3}$$

3.3. Approximated 3D equivalent thermomechanical loadings

Step 3 (Fig. 4d): based on the approximated 2D thermomechanical loadings in each section $S_{(i)}$, it is possible to build the 3D thermomechanical loadings on the machined surface. These loadings can take the form of a distribution via Eqs. (4)–(6).

$$\varphi_{th-3D-appro(i)} = f(X, Y, Z) \tag{4}$$

$$\sigma_{n-3D-appro(i)} = f(X, Y, Z) \tag{5}$$

$$\sigma_{t-3D-appro(i)} = f(X, Y, Z) \tag{6}$$

3.4. Macroscopic forces

Step 4 (Fig. 4e): from the numerical simulations of orthogonal cutting in each section $S_{(i)}$, the cutting force $DF_{Y(NUM)}(i)$ and the penetration force $DF_{eX(NUM)}(i)$ can be obtained (Fig. 8). By summing all the elementary cutting forces $DF_{Y(NUM)}(i)$ and elementary penetration forces $DF_{eX(NUM)}(i)$ of each section $S_{(i)}$, it is possible to calculate the numerical macroscopic cutting force $F_{Y-TOT(NUM)}$ and penetration force $F_{eXX(NUM)}$ induced by each of the tool teeth (Eqs. (7)–(9)).

NB: To obtain the numerical macroscopic penetration force $F_{eXX(NUM)}$, it is necessary to introduce the elementary penetration forces $DF_{eX(NUM)}(i)$ into the reference system $S_R = (O, \vec{X}, \vec{Y}, \vec{Z})$, even though they have been identified in the system, $S_{L(i)} = (M_{(i)}, \vec{e}_X, \vec{Y}, \vec{e}_Z)$ (Fig. 8).

$$F_{Y-TOT(NUM)} = \sum_{i=1}^{n} F_{Y(NUM)}(i) \tag{7}$$

$$F_{eXX(NUM)}(i) = \overrightarrow{F_{eX(NUM)}(i)} \bullet \vec{X} = F_{eX(NUM)}(i) \bullet cos(\theta_{(i)}) \tag{8}$$

$$F_{eXX-TOT(NUM)} = \sum_{i=1}^{n} F_{eXX(NUM)}(i) \tag{9}$$

3.5. Calibration of 3D equivalent loadings

Step 6 (Fig. 4f): the approximate 3D thermomechanical loadings defined in Section 3.3 were proposed through orthogonal cutting simulations. It has been established that these simulations do not quantitatively predict the macroscopic forces [16]. It is proposed to calibrate the 3D thermomechanical loadings using the experimental values of the $F_{Y(EXP)}$ and $F_{X(EXP)}$ forces. Thus, the calibration coefficients G_{FY} and G_{FX} can be defined as:

$$G_{FY} = \frac{F_{Y(EXP)}}{F_{Y-TOT(NUM)}} \tag{10}$$

$$G_{FX} = \frac{F_{X(EXP)}}{F_{eXX-TOT(NUM)}} \tag{11}$$

The calibration coefficients require the measurement of the experimental forces generated by each of the teeth of the reamer. This leads to two difficulties. First, the reamer has 6 teeth. It is, therefore, necessary to isolate the effect of a single tooth. Secondly, the tool is symmetrical, which makes it difficult to access the radial components, as they compensate each other. To solve these two problems, an experimental set-up was developed by [17], as presented in Fig. 9a. The part studied is cut by electrical discharge machining into two parts: a blue part and a red part (Fig. 9b). The whole (blue part + red part) is reamed according to the hole making sequence. The blue part is small, to ensure that it is in contact with a single tooth of the reamer. It is fastened to a dynamometer, to measure the penetration force produced by a single tooth in the X direction and the cutting force in the Y direction. The red part is fixed on a stiff support. More details about this set-up can be found in the article [17].

Fig. 10 shows an example of 3D thermomechanical loadings calibrated from Eqs. (12)–(14). It corresponds to the case study presented in Section 4.

$$Heat\ flux\ density : \varphi th - 3D_{(calibrated)} = G_{FY} \bullet \varphi th - 3D - appro \tag{12}$$

$$Normal\ pressure : \sigma n - 3D_{(calibrated)} = G_{FX} \bullet \sigma n - 3D - appro \tag{13}$$

$$Tangential\ pressure : \sigma t - 3D_{(calibrated)} = G_{FY} \bullet \sigma t - 3D - appro \tag{14}$$

3.6. Thermomechanical simulation (residual stress modelling)

Step 7 (Fig. 4g): the last step of the methodology (Fig. 10) is the application of calibrated 3D thermomechanical loadings on the machined surface. These loadings move in the cutting direction at the cutting speed V_c. The model for the application and displacement of the thermomechanical loadings is developed in the finite element software SYSWELD® using an implicit formulation. The dimensions and mesh of

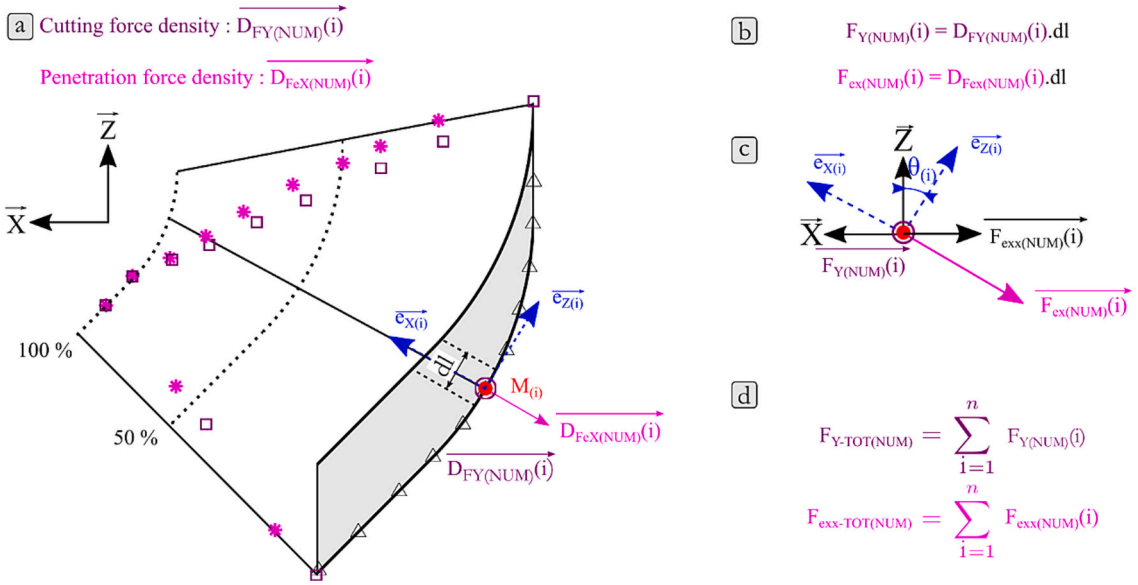

Fig. 8. Macroscopic numerical forces for an undeformed cut section CS and force distribution extracted from 2D ALE models.

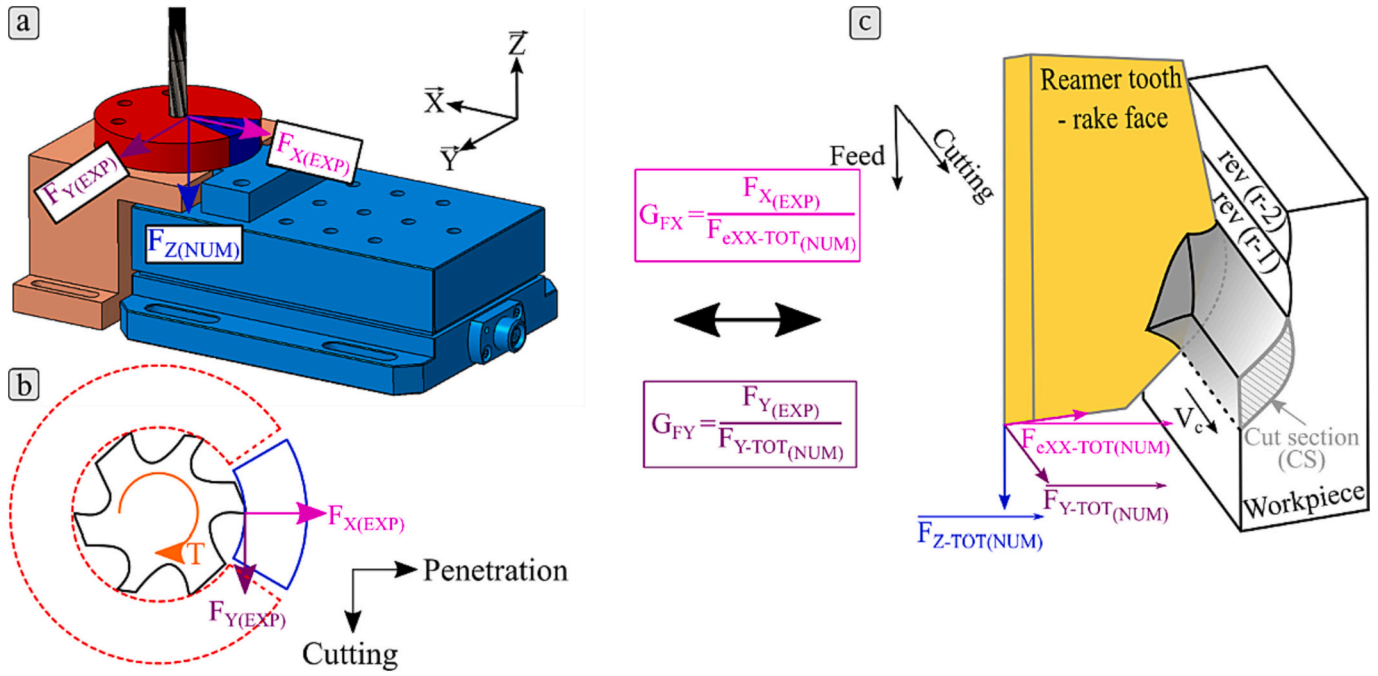

Fig. 9. Comparison of experimental (a and b) and macroscopic numerical forces (c) to obtain macroscopic force calibration coefficients.

the 3D model are shown in Fig. 11. The boundary conditions consist of mechanically locking all faces in all three directions, except the face where thermomechanical loadings are applied. Heat transfers are also allowed to model the conduction phenomenon with the bulk of the part and the heat exchange with the external environment (air and liquid).

The first step consists of moving a first loading. During the loading application, the surface is plastically deformed and the temperature increases, then decreases. At the end of the loading, the temperature has not returned to room temperature in the whole volume. The temperature continues to decrease over time because of the diffusion in the bulk of the part via the boundaries of the model. However, the cooling of the machined part is probably not complete because the thermomechanical loading of the next tooth arrives very quickly (6 teeth $\geq$ 6 loadings per revolution of the tool). These successive loadings interact with each other, as explained by [12]. It is necessary to simulate the passage of several teeth to obtain a stable state of residual stresses. Indeed, the thermomechanical loadings applied by the tooth (r) affect the residual state obtained after the previous teeth (r-1), (r-2) etc. Thus, to simulate several teeth and several revolutions, the model is geometrically modified between two revolutions to take into account the material removal. Between each tooth, the residual stress field generated by the previous tooth must be transferred to the simulation of the next tooth loading (more details can be found in [16]).

NB: Fig. 12 illustrates the need to take 2 phases into account. In the first phase, the cutting time $t_{cutting}$ is expressed in seconds and corresponds to the duration for a tooth to cross the length T of the simulated part (in red in Fig. 12). The tool moves at the cutting speed V_c. Then, the second phase corresponds to the cooling time $t_{cooling}$ between the end of the machining by the tooth (r) and the beginning of the machining of the next tooth (r + 1). During this period $t_{cooling}$ (s), there is no contact between the teeth and the simulated part. These two times are calculated by Eqs. (15) and (16).

$$t_{cutting} = \frac{60 \times T}{1000 \times V_c} \tag{15}$$

$$t_{cooling} = \frac{60 \times (\pi \times D - T)}{1000 \times Z \times V_c} \tag{16}$$

D is the diameter of the hole (mm), T is the thickness of the 3D model (mm) (Fig. 11) and Z is the number of teeth of the reamer.

4. Validation of the model with a case study

The aim of this section is to apply the modelling method to a case study.

4.1. Case study and experimental results

The reamer is presented in Fig. 2. It had a diameter of 15 mm and was made of tungsten carbide with a TiAlN coating. It had 6 teeth, a rake angle $\gamma_n = 6°$, a clearance angle $\alpha_n = 1°$, a cutting edge radius $R_\beta = 10$ µm, a corner radius $R_\varepsilon = 80$ µm and a lead angle $\kappa_r = 45°$. Regarding the cutting conditions, the cutting speed V_c was set to 5 m/min, the feed f to 0.18 mm/rev and the depth of cut a_p to 0.05 mm. Abundant lubrication was used during the testing.

The objective of this work was to simulate the influence of the 6 main cutting edges of the tool. The effect of the margins was not considered. A reamer with a high back taper angle ($\kappa'_r = 0.23°$) was designed to limit the contact between the margins and the machined surface. Moreover, the proposed model only simulated the descent of the reamer into the hole and not the ascent. So as to be consistent, the reaming operation was stopped in the lower position when the reamer had completed its work. The reamer was manually removed in the bottom direction, to avoid any additional contact with the machined surface.

The reaming operation was performed on 15-5PH martensitic stainless steel parts within a H1025 state (annealing at 1025 °C during 4 h).

It was assumed that the part did not contain residual stresses induced by the previous manufacturing operations. To be consistent with this assumption, a relaxation heat treatment was applied to the samples. In addition, prior to the reaming operation, the samples were drilled and bored until they reached a diameter of 14.9 mm. [6] showed that these roughing operations do not influence the residual stresses generated by the reaming operation (Fig. 1). Thus the part is assumed to be free from residual stresses.

After the reaming operation, the characterisation of residual stresses in a hole is not a turn-key method and X-ray diffraction techniques cannot be used directly. The protocol developed by [20] (Fig. 13) was

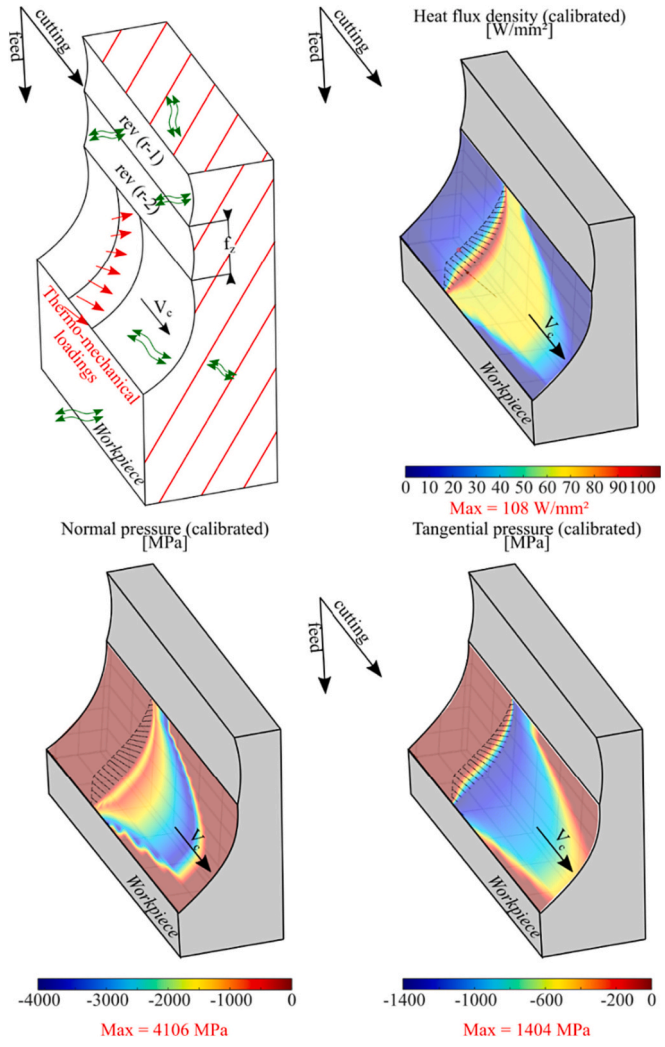

Fig. 10. 3D thermomechanical calibrated loadings.

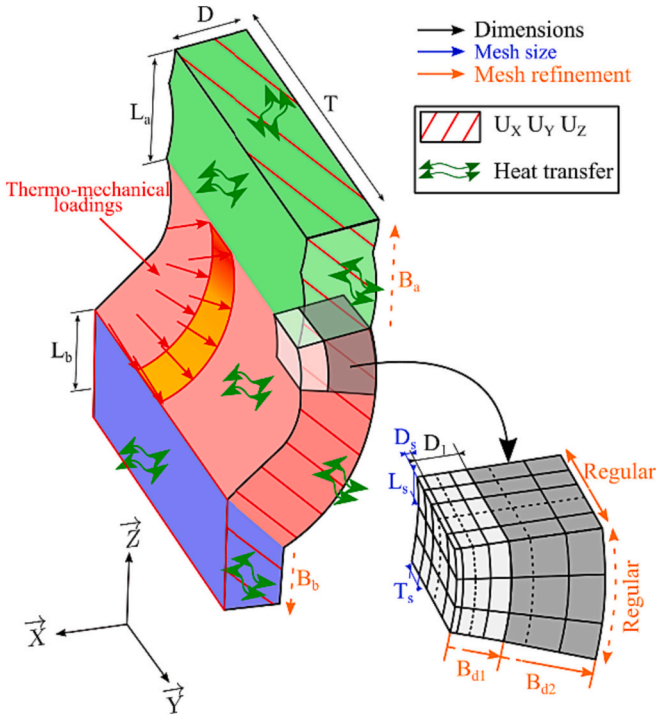

Fig. 11. Residual stress thermomechanical model description: element mesh size, dimensions and boundary conditions.

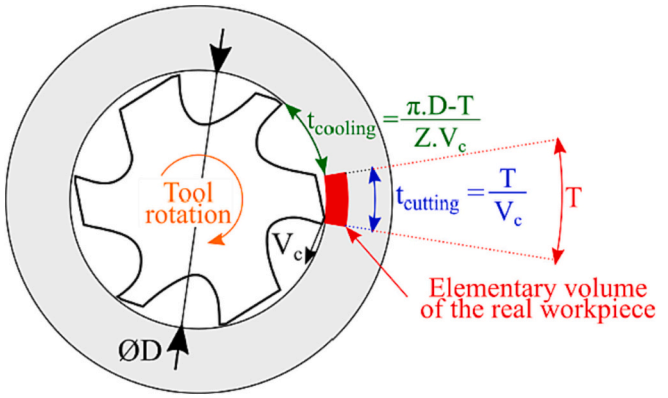

Fig. 12. Presentation of the cutting and cooling time.

applied. It consisted of applying a heat treatment (Fig. 13b), then milling the upper surface (Fig. 13c), and then performing the machining range (drilling, boring and, finally, reaming). The sample was cut gently with a hand saw to limit heating. The machined surface was then accessible for residual stress evaluation by X-ray diffraction in the axial and circumferential directions.

The X-ray measurements have been performed with a XRD system provided by the PROTO company, using a MGR40 head and equipped with a 2-mm diameter collimator.

Diffraction conditions:

- Cr Kα Radiation with 18 kV, 4 mA
- $\lambda = 0.229$ nm, plans {211}
- Bragg's Angles: $2\theta = 155{,}00°$
- Ω acquisition mode

Acquisition conditions:

- 7 β-angles (from −30° to +30°) in both directions X and Y
- β Oscillations: ± 6°

Stress calculation:

- Elliptic treatment method
- Radio crystallographic elasticity constants: ½ $S_2 = 5.92 \times 10^{-6}$ MPa^{-1} /$S_1 = -1.28 \times 10^{-6}$ MPa^{-1}

The in-depth residual stress distribution has been investigated after successive layer removal by means of an electrochemical polishing system.

Three samples were manufactured with the same manufacturing conditions so as to evaluate the natural deviation of the reaming process. The 3 residual stress profiles are plotted in Fig. 14.

It can be seen that the surface machined by the reamer had a compressive stress in the range of −600 to −800 MPa in the axial direction, and −300 to −500 MPa in the circumferential direction. Further down, the stress profile rose towards its initial state (stress free) and the affected depth was of the order of 100 µm. One can observe deviation between the 3 stress profiles, which illustrates natural experimental deviation. According to [3], the shape of these compressive residual stress profiles suggests that the reaming process is essentially driven by mechanical phenomena (plasticity). Indeed, in processes where thermal heating is dominant, the residual stress state is, preferentially, in tension.

4.2. Numerical results

4.2.1. 2D ALE modelling in Abaqus explicit

Section 4.1 introduced the step of the discretisation of the

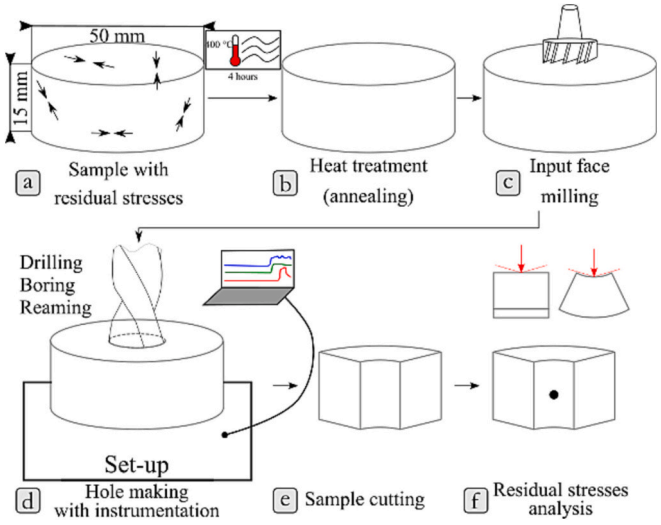

Fig. 13. Experimental protocol designed by Girinon [20].

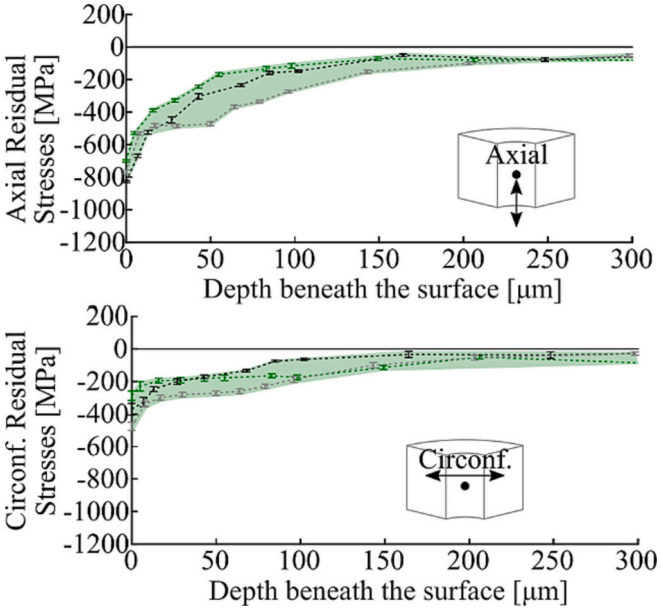

Fig. 14. Residual stresses measured experimentally.

undeformed cut section *CS* (Fig. 4b) into several sections $S_{(i)}$. For each section $S_{(i)}$, it is necessary to perform a 2D orthogonal cutting simulation using ABAQUS Explicit (assumption of plain strain without any interactions among the neighbouring sections), with an undeformed cut thickness of $h_{(i)}$ (Fig. 6). It was decided to divide the undeformed cut section *CS* into $n = 10$ elementary $S_{(i)}$ sections. In practice, it is not useful to simulate the 10 conditions of $h_{(i)}$ because several sections almost have the same thickness $h_{(i)}$; 3 to 5 simulations are sufficient. In this case study, 3 thicknesses were simulated: $h_{(1)} = 10$ µm, $h_{(2)} = 25$ µm and $h_{(3)} = 40$ µm. The thermomechanical loadings for the remaining values of $h_{(i)}$ were then interpolated to build the 3D thermomechanical loadings for the 10 sections.

For the orthogonal cutting model in ABAQUS Explicit, the thermophysical properties of the workpiece (15-5PH steel) and the cutting tool (carbide) are listed in Table 1 and Table 2. These properties have been previously identified by [12].

In the literature, there is no friction law for the TiAlN (tool coating) rubbing against the 15-5PH steel (work material). [12] identified a friction law for a TiN coating rubbing against a 15-5PH. It is assumed

Table 1
Thermophysical properties of the 15-5PH material.

Parameters	Temperature [°C]	Value
Thermal conductivity λ [W.m^{-1}.°C^{-1}]	0	8.7
	1200	29.2
Specific heat C [J.kg^{-1}.°C^{-1}]	0	248
	1200	1400
Density ρ [kg.m^3]	0	7810
	1200	7450
Young's Modulus E [MPa]	0	197,000
	1200	128,600
Thermal expansion coefficient α [°C^{-1}]	−73	0.0000104
	1200	0.0000145
Poisson's coefficient ν [−]		0.272

Table 2
Thermophysical properties of the tool carbide substrate.

Parameters	Value
Thermal conductivity λ [W.m^{-1}.°C^{-1}]	110
Specific heat C [J.kg^{-1}.°C^{-1}]	288
Density ρ [kg.m^3]	14,600
Young's Modulus E [MPa]	620,000
Thermal expansion coefficient α [°C^{-1}]	0.0000049
Poisson's coefficient ν [−]	0.235

that the TiAlN coating has similar friction properties to the TiN coating. This tribological system has been shown to exhibit a high value of friction coefficient (0.8) at low sliding speed. As the cutting speed is very low in reaming (Vc = 5 m/min), it is assumed that the friction coefficient remains constant at 0.8 [12] in the proposed model.

A Johnson-Cook flow stress constitutive equation, identified by [12], was used to model the mechanical behaviour of 15–5 PH (Table 3, Eq. (17)).

$$\sigma_{eq} = \left[A + B.\epsilon_p^n\right] \bullet \left[1 + C.ln\left(\frac{\dot{\epsilon}_p}{\dot{\epsilon}_0}\right)\right] \bullet \left[1 - \left(\frac{T - T_0}{T_m - T_0}\right)^m\right] \quad (17)$$

where ϵ_p^n is the current plastic strain, $\dot{\epsilon}_p$ is the plastic strain rate [s^{-1}], $\dot{\epsilon}_0$ is the reference plastic strain [s^{-1}], A is the yield strength [MPa], B is the strain hardening modulus [MPa], n is the hardening coefficient, C is the strain rate sensitivity coefficient, m *is* the thermal softening coefficient, T is the current temperature [°C], T_0 is the room temperature [°C] and T_m is the melting temperature [°C]. From a rheological point of view, three terms can be distinguished in the equation; the first represents the elasto-plasticity, the second the viscosity, and the third, the thermal softening.

At the end of the 3 simulations for the 3 values of $h_{(i)}$, the 3 thermal and mechanical loadings for each of the 3 sections were plotted in Fig. 15: the heat flux distribution $\varphi_{th-2D-ext(i)}$, tangential stress $\sigma_{t-2D-ext(i)}$, and normal stress $\sigma_{n-2D-ext(i)}$. From this, the loadings for the remaining 7 sections were interpolated ($7 + 3 = n = 10$). The 3D thermomechanical loadings can be approximated by juxtaposing the 10 thermomechanical loadings. Their shapes are illustrated in Fig. 10.

4.2.2. Calibration of the 3D thermomechanical loadings

The intensity of the 3D thermomechanical loadings must be calibrated using experimental force measurements. The forces produced by a single tooth on the workpiece were measured via the test bed described in Section 3.5 and in [17] (Fig. 9). On average, the tangential cutting

Table 3
Flow stress model: Johnson-Cook parameters for 15-5PH.

A [MPa]	B [MPa]	n	C	$\dot{\epsilon}_0$	m	T_m [°C]	T_0 [°C]
855	448	0.14	0.0137	1	0.63	1440	20

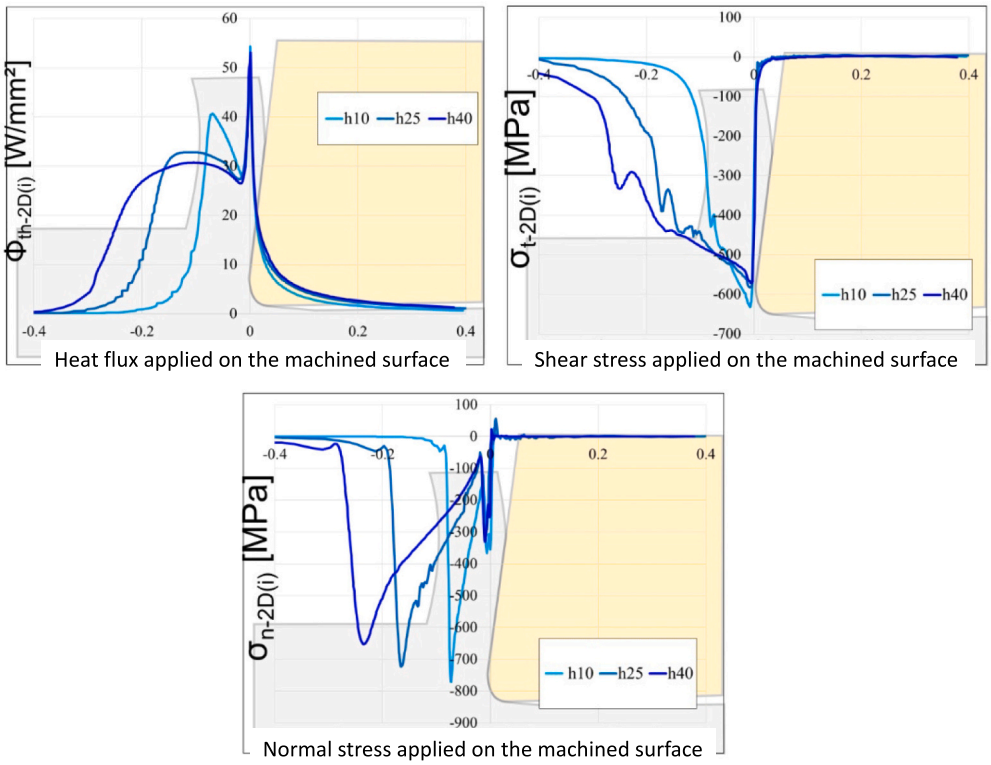

Fig. 15. 2D thermomechanical loadings extracted from ABAQUS for 3 uncut chip thicknesses.

force $F_{Y(EXP)}$ is 18 N and the penetration force $F_{X(EXP)}$ is 23 N, in the radial direction reported in Table 4.

The numerical cutting forces $F_{Y\text{-}TOT(NUM)}$ and penetration $F_{eXX\text{-}TOT(NUM)}$ are calculated from the 3D orthogonal cutting simulations as presented in Section 3.4 (Fig. 8). It was then possible to calculate the calibration coefficients G_{FY} and G_{FX} (defined in Section 3.5). It is confirmed that the ABAQUS simulations underestimate the forces, which was already observed by [16]. The estimation of the cutting force is closer to reality ($G_{FY} = 2.23$) than the penetration force ($G_{FX} = 5.15$), which is a common weak point of the orthogonal cutting simulations as reported by [21]. The calibrated 3D thermomechanical loadings were then determined and illustrated in Fig. 10.

4.2.3. 3D residual stress modelling in SYSWELD

The thermomechanical loadings were applied and moved in the model developed in SYSWELD and the meshing conditions are summarised in Table 5 and Fig. 11.

Most of the thermophysical properties of the material parts are the same as those presented for the ABAQUS model. The air/part heat exchange coefficient was set to 5000 $W.m^{-2}.°C^{-1}$ and the heat transfer to the mass of the material was allowed with a coefficient set to 2000 $W.m^{-2}.°C^{-1}$. These values are in accordance with the previous work of [12].

However, the constitutive equation of the workmaterial 15-5PH used in SYSWELD was different from the one used in the ABAQUS cutting model. Indeed, it is necessary to take into account the cyclic thermomechanical loading/unloading, which is based on the Von-Mises elastoplastic behaviour law associated with a kinematic strain hardening law from Armstrong Frederik (Eqs. (18)–(19)). This model was identified by [12] by cyclic testing and the parameters are summarised in Table 6.

Table 4
Comparison between the experimental and the numerical forces - Calibration coefficients obtained.

	Exp	Num	G_{FY}	G_{FX}
Cutting direction	$F_{Y(EXP)}$ 18 N	$F_{Y\text{-}TOT(NUM)}$ 8 N	2.23	
Penetration direction	$F_{X(EXP)}$ 23 N	$F_{eXX\text{-}TOT(NUM)}$ 4.5 N		5.15

Table 5
3D mesh parameters corresponding to Fig. 11.

Dimensions [mm]	L_a	L_b	D	T
	0.40	0.20	0.05	0.30
Mesh size [mm]	L_s	D_s	T_s	D_1
	0.005	0.003	0.003	0.150
Mesh refinement [−]	B_a	B_b	Bd1	Bd2
	1.0	1.0	1.2	1.6

$$f = \sqrt{3J_2(\bar{\bar{\sigma}} - \bar{\bar{\chi}})} - \sigma_y \tag{18}$$

$$\dot{\chi} = \frac{2}{3}C\dot{\epsilon^p} - \gamma\bar{\bar{\chi}}\dot{p} \tag{19}$$

where C and γ are material parameters, σ_y is the yield strength and p is the plastic strain defined by Eq. 20. The values are presented in Table 6.

$$\dot{p} = \sqrt{\frac{2}{3}\dot{\epsilon^p} : \dot{\epsilon^p}} \tag{20}$$

It is necessary to simulate the passage of 13 teeth (k = 13 in Fig. 16a)

Table 6
Flow stress model - Armstrong Frederik hardening law parameters for 15-5PH [12].

Temperature [°C]	σ_y [MPa]	C	γ
20	530	421,405	730
300	382	284,420	508
600	197	120,000	600

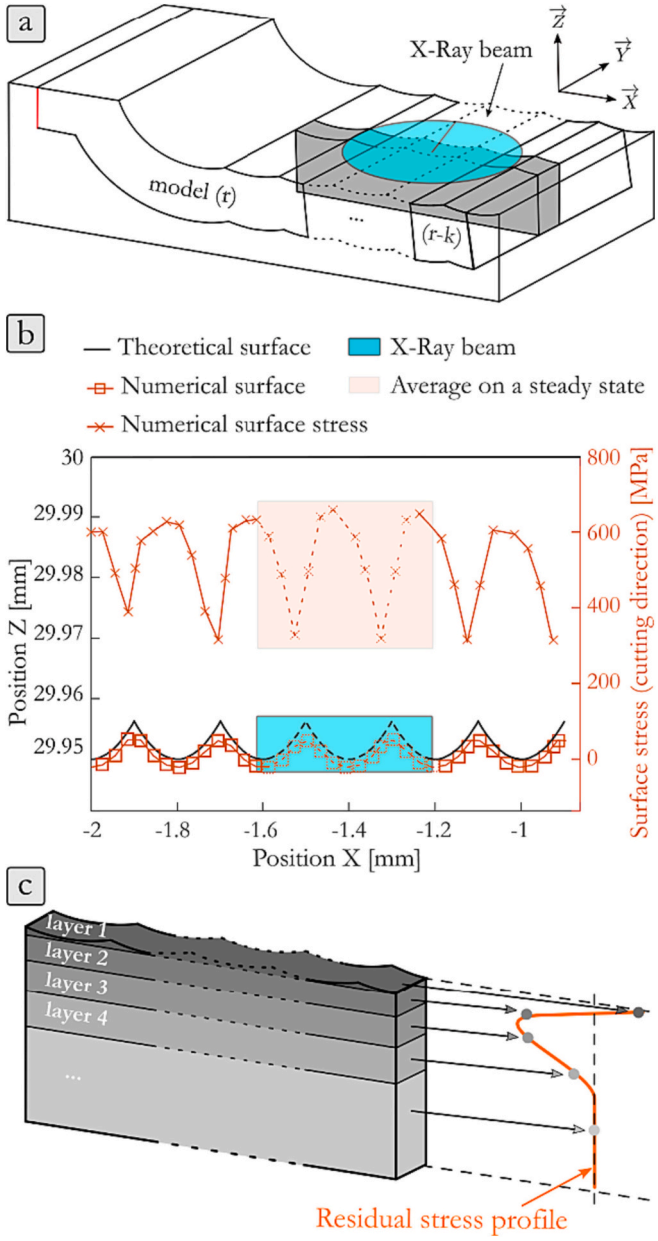

Fig. 16. Numerical residual stress profiles building methodology, a) model overlapping of successive revolutions, b) surface stress average on a stabilised zone, c) in-depth average layer by layer for residual stress profile building [16].

to reach a steady state of residual stress generation. This first result highlights that it is necessary to wait for about 2 revolutions (2 revolutions = 2 × 6 teeth/rev) of the reamer to reach this steady-state. The number of simulations (=passage) is much higher than the turning case simulated by [16] (5 revolutions in turning with a single cutting edge ⇔ 13 passages in reaming). This shows that there is a lot of interactions between the various passages of the cutting teeth. This is the consequence of the small feed, that leads to a small average chip thickness and to the high loading frequency (small diameter + 6 teeth ⇔ large diameter in turning with a single edge).

Fig. 16b shows the theoretical roughness profile and the residual stress profile (cutting direction) simulated by the model. It is well known that residual stresses vary along the axial direction [22]. The frequency of the roughness profile corresponds to the feed per tooth. In the steady-state zone, the numerical residual stresses are averaged over 3 tooth passages (0.09 mm wide zone). It should be noted that the experimental measurements are averaged over a larger area (width of the XRD spot = 2 mm) (Fig. 16a). Fig. 16c reminds that the method developed by [16] evaluates the stresses over several depths until the initial residual stress state is found.

4.3. Comparison of residual stress profiles

Fig. 17 shows the comparison between the residual stresses predicted by the model in both axial and circumferential directions, and the cloud of experimental values already presented in Fig. 14. The numerical residual stresses show a good consistency with the experimental values. It should be noted that the model predicts the compressive stress state in both directions well. It also predicts the affected depth, of the order of 100–150 µm. As reported by [3], such residual stress profiles are the consequence of machining processes in which plastic deformation is the dominant mechanism, compared to thermal phenomena.

It is possible to compare the residual stress profiles generated by turning and by reaming for the same work material 15-5PH in Fig. 18. The residual stresses in turning are reported from the work of [16] with the following cutting conditions: Vc = 120 m/min – f = 0.2 mm/rev – a_p = 0.2 mm/rev. In turning the residual stress profiles are in tension in the near surface. Indeed, the high cutting speed is supposed to lead to a much larger amount of heat generated in the surface, which is in favor of tensile stresses in the surface since [3]. On the contrary, reaming uses very low cutting speeds (Vc = 5 m/min) which induces a small amount of thermal energy. This analysis is confirmed by the analysis of the heat flux distribution and especially the maximum heat flux density that is of the order 100 W/mm^2 in reaming (Fig. 10), whereas it is 300 % higher in turning around 300 W/mm^2 [16].

As far as the mechanical loadings are concerned, it can be stated that the normal stress distribution, and especially its maximum value is of the order of 4.1 GPa in reaming (Fig. 10), whereas it is of 3.1 GPa in turning [16]. Both values are within the same order of magnitude. However, reaming leads to a more severe mechanical loading. So, it can be concluded that the residual stress generation in reaming is mainly dominated by mechanical phenomena; i.e. plastic deformation.

It should be reminded that this first version of the model only considers the effect of the main cutting edges and neglect the influence of the secondary cutting edges and of the margins. The secondary cutting edges can generate an additional cut (few micrometers) or a rubbing effect, that may disturb the residual stress state. In the present paper, this hypothesis is consistent with the use case in which a reamer having a high back taper angle has been involved. However, industry also uses reamers having a low back taper angle. So, it is of interest to investigate the influence of the secondary cutting edges in a future work.

5. Conclusions

This paper presents a numerical model for predicting the residual stress state generated by a reaming operation with a solid multi-tooth reamer. The model simulates the influence of main cutting edges using equivalent thermomechanical loadings. These 3D thermomechanical loadings are juxtaposed thanks to several 2D orthogonal cutting simulations. The 3D thermomechanical loadings are then calibrated by experimental stress measurements during an actual reaming operation. Finally, the model applies thermomechanical loadings induced by all the teeth for several revolutions until a steady state is reached for residual stress generation. Numerical results are in good agreement with the residual stresses obtained experimentally. The model highlights that a reaming operation has a significant effect on the residual stress state at the surface, and that its action is dominated by plastic deformation, leading to compressive stresses.

Funding

This research was supported by the companies Airbus Helicopters,

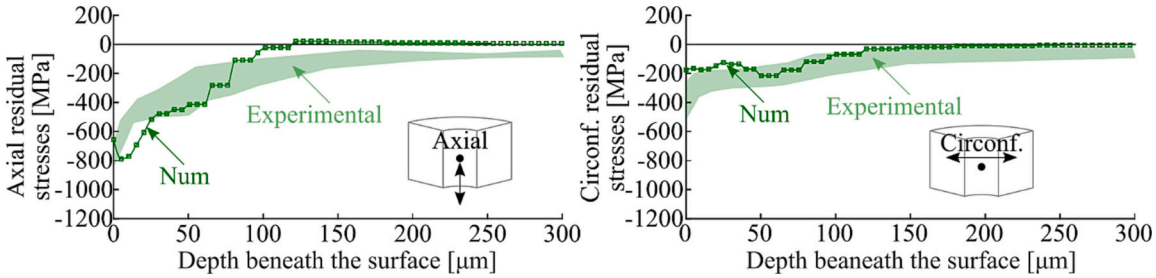

Fig. 17. Residual stress comparison for the numerical model validation: experimental results displayed in light green and numerical results in dark green. (For interpretation of the references to colour in this figure legend, the reader is referred to the web version of this article.)

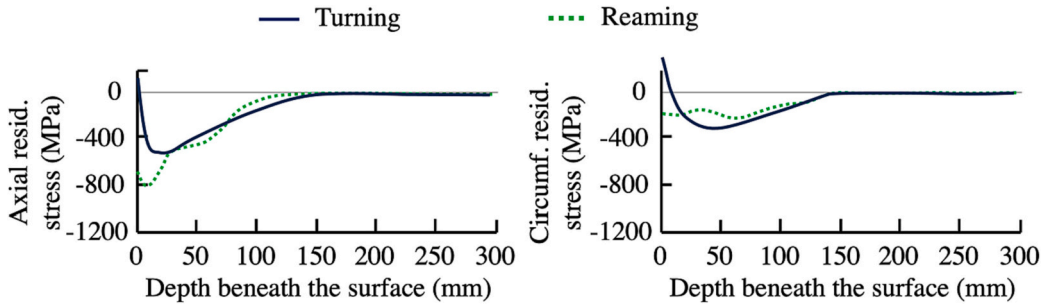

Fig. 18. Comparison between the numerical residual stress induced by a turning and a reaming operation in a 15-5PH stainless steel.

Safran, Framatome, Cetim and ANR.

Code availability

The code generated during the current study is not available.

Ethics approval

Not applicable.

Consent to participate

Not applicable.

Consent for publish

Not applicable.

Declaration of competing interest

The authors declare that they have no known competing financial interests or personal relationships that could have appeared to influence the work reported in this paper.

Data availability

The data generated during and/or analyzed during the current study are available from the corresponding author on reasonable request.

Acknowledgments

Authors are thankful to the French National Research Agency (ANR), as well to Airbus Helicopters, Safran, Framatome and Cetim for their financial support in the MISU Chair program. Authors would also acknowledge M. Cici, H. Pascal, H. Seux and P. Polly from ENISE for their valuable support regarding the machining of samples and XRD analysis.

References

[1] Smith S, Melkote SN, Lara-Curzio E, Watkins TR, Allard L, Riester L. Effect of surface integrity of hard turned AISI 52100 steel on fatigue performance. Mater Sci Eng A 2007;459(1–2):337–46. https://doi.org/10.1016/j.msea.2007.01.011.
[2] Griffiths B. Manufacturing surface technology - surface integrity and functional performance. Penton Press; 1971 [ISBN 1-56032-970-X.].
[3] Rech J, Hamdi H, Valette S. Workpiece surface integrity. In: Machining: fundamentals and recent advances. London: Springer; 2008. p. 59–96. https://doi.org/10.1007/978-1-84800-213-5-3.
[4] Kang J, Steven Johnson W, Clark DA. Three-dimensional finite element analysis of the cold expansion of fastener holes in two aluminum alloys. J. Eng. Mater. Technol. 2002;124(2):140–5. https://doi.org/10.1115/1.1448922.
[5] Lacombe A, Landon Y, Paredes M, Chirol C, Benaben A. Numerical simulation of the reaming process in aluminium 2024-T351 - analysis of the evolution of the material stress state. Dyna (Spain) 2019;94(3):215–20. https://doi.org/10.6036/9010.
[6] Leveille T, Granier C, Valiorgue F, Pascal H, Rech J, Van-Robaeys A, et al. Characterization of residual stresses induced by a multistep hole making sequence. Procedia CIRP 2021;102:477–81. https://doi.org/10.1016/j.procir.2021.09.081.
[7] Ulutan D, Ozel T. Machining induced surface integrity in titanium and nickel alloys: a review. Int J Mach Tool Manuf 2011;51:250–80. https://doi.org/10.1016/j.ijmachtools.2010.11.003.
[8] Shet C, Deng X. Residual stresses and strains in orthogonal metal cutting. Int J Mach Tool Manuf 2003;43:573–87. https://doi.org/10.1016/S0890-6955(03)00018-X.
[9] Ee K, Dillon O, Jawahir I. Finite element modeling of residual stresses in machining induced by cutting using a tool with finite edge radius. Int. J. Mech. Sci. 2005;47:1611–28. https://doi.org/10.1016/j.ijmecsci.2005.06.001.
[10] Liu CR, Guo Y. Finite element analysis of the effect of sequential cuts and tool-chip friction on residual stresses in a machined layer. Int. J. Mech. Sci. 2000;42:1069–86. https://doi.org/10.1016/S0020-7403(99)00042-9.
[11] Nasr MN, Ng EG, Elbestawi M. Modelling the effects of tool-edge radius on residual stresses when orthogonal cutting AISI 316l. Int J Mach Tool Manuf 2007;47:401–11. https://doi.org/10.1016/j.ijmachtools.2006.03.004.
[12] Mondelin A, Valiorgue F, Rech J, Coret M, Feulvarch E. Hybrid model for the prediction of residual stresses induced by 15-5PH steel turning. Int. J. Mech. Sci. 2012;58(1):69–85. https://doi.org/10.1016/j.ijmecsci.2012.03.003.
[13] Attanasio A, Ceretti E, Giardini C. 3D FE modelling of superficial residual stresses in turning operations. Mach. Sci. Technol. 2009;13:317–37. https://doi.org/10.1080/10910340903237806.
[14] Liu Y, Weng J, M'Saoubi R, Ahadi A, Zhou J. Evolution of residual stress when turning a fillet radius in stainless steel. J. Manuf. Process. 2023;85:216–26.
[15] Valiorgue F, Rech J, Hamdi H, Gilles P, Bergheau J. A new approach for the modelling of residual stresses induced by turning of 316L. J Mater Process Technol 2007;191:270–3. https://doi.org/10.1016/j.jmatprotec.2007.03.021.
[16] Dumas M, Fabre D, Valiorgue F, Kermouche G, Van Robaeys A, Girinon M, et al. 3D numerical modelling of turning-induced residual stresses – a two-scale approach

based on equivalent thermo-mechanical loadings. J Mater Process Technol 2021; 297(117274). https://doi.org/10.1016/j.jmatprotec.2021.117274.

[17] Leveille T, Valiorgue F, Claudin C, Rech J, Van-Robaeys A, Masciantonio U, et al. Influence of the reaming process on hole's surface integrity and geometry in a martensitic stainless steel 15-5PH. Procedia CIRP 2022;108:384–9. https://doi.org/10.1016/j.procir.2022.03.062.

[18] Courbon C, Mabrouki T, Rech J, Mazuyer D, Perrard F, D'Eramo E. Further insight into the chip formation of ferritic-pearlitic steels: microstructural evolutions and associated thermo-mechanical loadings. Int J Mach Tool Manuf 2014;77:34–46. https://doi.org/10.1016/j.ijmachtools.2013.10.010.

[19] Rech J, Battaglia JL, Moisan A. Thermal influence of cutting tool coatings. J Mater Process Technol 2005;159(1):119–24. https://doi.org/10.1016/j.jmatprotec.2004.04.414.

[20] Girinon M, Valiorgue F, Rech J, Feulvarch E. Development of a procedure to characterize residual stresses induced by drilling. Procedia CIRP 2016;45:79–82. https://doi.org/10.1016/j.procir.2016.02.074.

[21] Arrazola PJ, Özel T, Umbrello D, Davies M, Jawahir IS. Recent advances in modelling of metal machining processes. CIRP Annals 2013;62(2):695–718. https://doi.org/10.1016/j.cirp.2013.05.006.

[22] Valiorgue F, Rech J, Hamdi H, Gilles P, Bergheau JM. 3D modeling of residual stresses induced in finish turning of an AISI304L stainless steel. Int J Mach Tool Manuf 2012;53(1):77–90. https://doi.org/10.1016/j.ijmachtools.2011.09.011.